

Development of macro-defect-free PBF-EB-processed Ti–6Al–4V alloys with superior plasticity using PREP-synthesized powder and machine learning-assisted process optimization

Yunwei Gui^{a,b}, Kenta Aoyagi^{b,*}, Akihiko Chiba^b

^a Department of Materials Processing, Graduate School of Engineering, Tohoku University, 6-6 Aramaki Aza Aoba, Aoba-ku, Sendai, 980-8579, Japan

^b Institute for Materials Research, Tohoku University, 2-1-1 Katahira, Aoba-ku, Sendai, 980-8577, Japan

ARTICLE INFO

Keywords:

Powder bed fusion using electron beams
Ti–6Al–4V alloys
Surface quality
Internal macro-defects
Support vector machine

ABSTRACT

The elimination of internal macro-defects is a key issue in Ti–6Al–4V alloys fabricated via powder bed fusion using electron beams (PBF-EB), wherein internal macro-defects mainly originate from the virgin powder and inappropriate printing parameters. This study compares different types powders by combining support vector machine techniques to determine the most suitable powder for PBF-EB and to predict the processing window for the printing parameters without internal macro-defects. The results show that powders fabricated via plasma rotating electrode process have the best sphericity, flowability, and minimal porosity and are most suitable for printing. Surface roughness criterion was also applied to determine the quality of the even surfaces, and support vector machine was used to construct processing maps capable of predicting a wide range of four-dimensional printing parameters to obtain macro-defect-free samples, offering the possibility of subsequent development of Ti–6Al–4V alloys with excellent properties. The macro-defect-free samples exhibited good elongation, with the best overall mechanical properties being the ultimate tensile strength and elongation of 934.7 MPa and 24.3%, respectively. The elongation of the three macro-defect-free samples was much higher than that previously reported for additively manufactured Ti–6Al–4V alloys. The high elongation of the samples in this work is mainly attributed to the elimination of internal macro-defects.

1. Introduction

Additive manufacturing (AM) technologies can rapidly manufacture complex or custom parts, reducing process steps and saving manufacturing time [1–4], and are widely used in the aerospace, automotive, and other precision industries [5,6]. Powder bed fusion using an electron beam (PBF-EB) is an additive manufacturing method that uses a high-energy electron beam to melt metal powders layer by layer to produce parts. In contrast to selective laser melting, PBF-EB involves the preparation of samples in a high vacuum environment, which effectively prevents the introduction of impurities such as O and N. It also involves a preheating process for the print substrate and powder, which reduces residual thermal stress on the sample and subsequent heat treatment processes [2–4,7]. Due to these features and advantages, PBF-EB technology is a very important AM technology with great potential in metallic materials. Moreover, PBF-EB is the ideal AM technology for the manufacture of complex components made of many alloys, such as

titanium alloys, nickel-based superalloys, aluminum alloys and stainless steels [2–4,8].

Ti–6Al–4V alloy is one of the prevalent commercial titanium alloys possessing high specific strength, excellent mechanical properties, excellent corrosion resistance, and good biocompatibility [9,10]. It is widely used in applications requiring low density and excellent corrosion resistance, such as the aerospace industry and biomechanical applications [11,12]. The mechanical properties of PBF-EB-processed Ti–6Al–4V alloys are superior to those fabricated by casting or forging, because the rapid cooling rate in PBF-EB results in finer grains [12–18]. However, the PBF-EB-fabricated parts often include internal macro-defects, which compromises their mechanical properties [19–22]. This study focused on the elimination of macro-defects, such as porosity, lack of fusion, incomplete penetration and unmelted powders, which distinguishes them from micro-defects such as vacancies, dislocations, grain boundaries and secondary phases, etc. Large-sized fusion defects cause a severe reduction in mechanical strength. Smaller defects,

* Corresponding author.

E-mail address: kenta.aoyagi.e7@tohoku.ac.jp (K. Aoyagi).

<https://doi.org/10.1016/j.msea.2023.144595>

Received 14 October 2022; Received in revised form 23 December 2022; Accepted 3 January 2023

Available online 5 January 2023

0921-5093/© 2023 Elsevier B.V. All rights reserved.

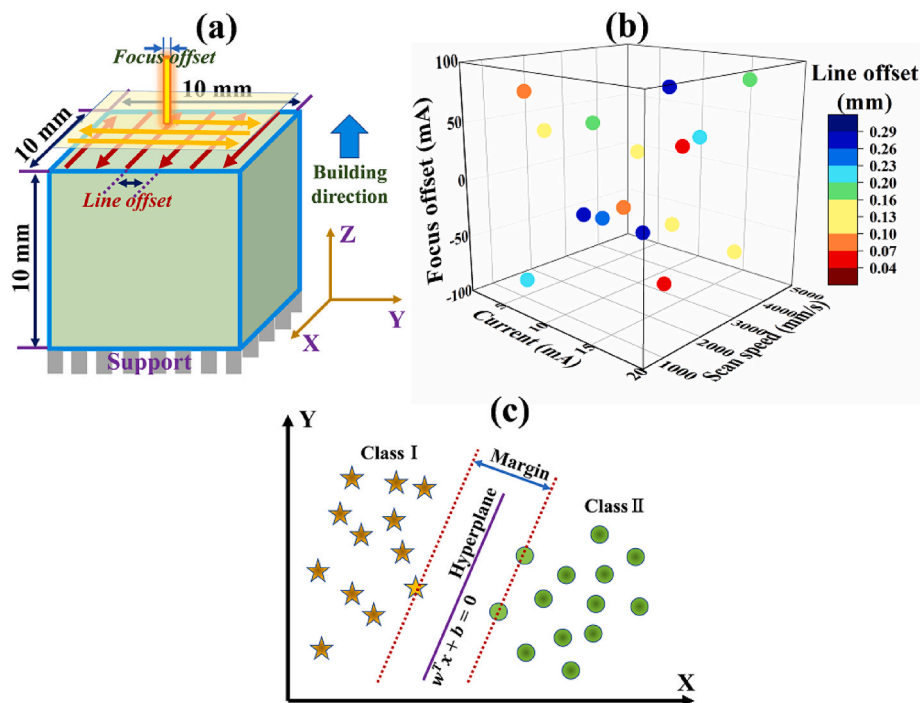


Fig. 1. (a) Schematic of the scan strategy and a component with dimensions $10 \times 10 \times 10 \text{ mm}^3$, (b) sixteen sets of four-dimensional printing parameters designed using a uniform experimental design, and (c) schematic of the proposed SVM model.

such as pores and cracks, lead to the initiation of fatigue cracking and rapidly accelerate the cracking process [23]. The issue of internal macro-defects must be addressed to expand the application of the PBF-EB technology. The main studies for controlling internal macro-defects are online monitoring of defects, remelting and hot isostatic pressing (HIP). The literatures [24,25] report the use of infrared imaging or other imaging techniques to identify defects, but the monitoring of smaller sized defects is still not adequate. And in some cases remelting does not reduce the internal macro-defects of the part, but instead causes coarsening of the microstructure and volatilization of some metal elements [23]. The HIP treatment does not completely eliminate the internal macro-defects, the original defect location may still act as a point of origin of the crack, and the subsequent treatment will consume more time and economic costs [23]. Therefore, optimizing suitable printing parameters to avoid internal macro-defects in printed parts at source is of great industrial value and research significance, and is an urgent issue in PBF-EB related technology.

There are two causes of internal macro-defects in the AM process: gas pores trapped in the virgin powder and the inappropriate printing parameters [7,23]. Gui et al. [26] classify internal macro-defects during PBF-EB process according to their shape, such as spherical defects, elongated shape defects, flat shape defects and other irregular shape defects. Of these, spherical defects mainly originate from raw material powders. Other shape defects mainly originate from lack of fusion or unmelted powders caused by unsuitable printing parameters, etc. The PBF-EB process requires powders with good flowability, and spherical powders are typically chosen as raw materials. The prevalent techniques for the fabrication of pre-alloyed powders are gas atomization (GA), plasma atomization (PA), and the plasma rotating electrode process (PREP) [27,28]. These methods yield powders with different characteristics that affect the subsequent fabrication. The selection of a suitable powder for PBF-EB is particularly important to produce Ti-6Al-4V alloys without internal macro-defects. The need to optimize several printing parameters such as beam current, scan speed, line offset, and focus offset make it difficult to eliminate internal macro-defects that occur during printing [23]. Most of the studies [11,12,22,29–33] on the optimization of AM processes for Ti-6Al-4V alloys have focused on

samples with a limited set of parameters (e.g., power–scan speed) and do not allow for the guidance and development of unknown process windows for macro-defect-free samples. In addition, process optimization remains a time-consuming problem, with the traditional ‘trial and error’ method demanding considerable time and economic costs. The development of a simple and efficient method to predict the processing window for alloys without internal macro-defects is a key issue. In recent years, machine learning techniques have increasingly been used in the field of additive manufacturing and materials development [34,36,37]. Aoyagi et al. [38] recently proposed a novel and efficient method based on a support vector machine (SVM) to optimize the two-dimensional process parameters (current and scan speed) and obtain PBF-EB-processed CoCr alloys without internal macro-defects. The method is one of the potential approaches toward effective optimization of more than two process parameters and makes it possible for the machine learning techniques to accelerate the development of alloys without internal macro-defects.

Herein, we focus on the elimination of internal macro-defects, such as pores, lack of fusion, etc., caused by raw powders and printing parameters. The Ti-6Al-4V powders produced by three different methods were compared, and the powder with the best sphericity, flowability, and minimal porosity was selected as the feedstock for subsequent printing. The relationship between the surface roughness and internal macro-defects in the Ti-6Al-4V components was also investigated. The combination of SVM and surface roughness indices (Sdr) predicted a wider four-dimensional processing window for obtaining Ti-6Al-4V alloys without internal macro-defects. Finally, we investigated the tensile properties of Ti-6Al-4V alloys at room temperature with different printing parameters, as well as the corresponding microstructures and fracture types.

2. Experimental details

2.1. Starting materials

Three types of Ti-6Al-4V alloy powders, produced by GA, PA, and PREP, were compared. The particle size distribution of the powders was

Table 1
Process parameters and line energy used in this study.

Sample No.	Beam Current/ mA	Scan Speed/ mm.s ⁻¹	Line Offset/ mm	Focus Offset/ mA	Line energy/J. mm ⁻¹
1	13.6	699	0.29	-2	1.17
2	19.1	3486	0.19	91	0.33
3	4.3	1240	0.21	-90	0.21
4	2.8	3712	0.24	-64	0.05
5	11.3	3974	0.04	21	0.17
6	10.1	1761	0.17	55	0.34
7	12.1	2582	0.26	-42	0.28
8	1.7	2325	0.14	32	0.04
9	6.3	946	0.07	80	0.40
10	8.7	2906	0.09	-31	0.18
11	15.9	3105	0.23	43	0.31
12	7.7	4559	0.27	67	0.10
13	18.1	1527	0.06	-55	0.71
14	16.9	2068	0.16	-17	0.49
15	14.7	4779	0.11	-80	0.18
16	5.1	4270	0.12	3	0.07

Table 2
Thermophysical characteristics of Ti-6Al-4V alloy and the coefficients for simulation model used in this study.

Name	Symbol and unit	Value
Density	ρ (g/cm ³)	4.42–3.75
Viscosity	μ (mPa • s)	3.5–2.06
Thermal conductivity	κ (W/m • K)	7–34.6
Specific heat	C_p (J/kg • K)	546–831
Heat transfer coefficient for fluid to void	h_{FV} (W/m ² • K)	1000
Emissivity	ϵ	0.40
Surface tension at T_L	γ_L (J/m ²)	1.53
Temperature coefficient of surface tension	$\frac{d\gamma}{dT}$ (J/m ² • K)	-0.00028
Stefan-Boltzmann constant	σ (W/m ² • K ⁴)	5.67e-08
Environment pressure	P_0 (MPa)	0.1
Environment temperature	T_0 (K)	298

determined using a laser particle size analyzer (LS230, Beckman Coulter, USA), and the flowability was measured using a Hall flowmeter (JIS-Z2502, Tsutsui Scientific Instruments Co., Ltd., Japan), according to the ASTM B213 standard. The powder morphology and internal macro-defects were determined using scanning electron microscopy (SEM, JEOL JCM-6000) and X-ray CT (Comscantecno Co., Ltd, Yokohama, Japan), respectively. 3D rendering of the X-ray CT data and analysis of the void volume fraction were performed using ExFact® VR software (Nihon Visual Science, Inc., Tokyo, Japan). The size of the defect was considered as its effective diameter, which was defined as the diameter of a sphere with a volume equal to that of the defect.

2.2. PBF-EB processing

Ti-6Al-4V cubic parts with dimensions of 10 × 10 × 10 mm³, as shown in Fig. 1(a), were printed on an SUS316L baseplate using the PBF-EB machine developed by the Technology Research Association for Future Additive Manufacturing. The acceleration voltage of the machine was set to 60 kV. The printing parameters, that is, beam current, scan speed, line offset and focus offset were set in the ranges 1–20 mA, 500–5000 mm/s, 0.030–0.300 mm, and -100 to +100 mA, respectively. A total of 16 sets of printing parameters with different beam currents, scan speeds, line offsets, and focus offsets were designed using a uniform experimental design method [39] to evenly distribute the data points across the high-dimensional printing parameter space, as shown in Fig. 1(b). The 16 sets of printing parameters and line energy are listed in Table 1. The powder bed preheating temperature was set to 1043 K to avoid a smoking phenomenon, which is powder-spreading caused by the electrostatic force between the powders. A support structure with a

height of 3 mm was fabricated on the base plate. The printing was performed using an XY scanning strategy in which the bidirectional scanning direction was rotated by 90° for each successive layer, with a layer thickness of 75 μm.

2.3. Materials characterization and performance tests

The surface topography was measured using a Keyence® VR-3200 wide-area 3D measurement system. We used the developed interface area ratio (Sdr) as the surface roughness index, which indicates how much the area has increased relative to a defined area. In our previous research [26], we used carbon steel to derive the quantitative criteria for judging surface quality based on surface roughness as follows: Sdr < 0.015 for an even surface. Samples with even surfaces can be easily separated out using Sdr < 0.015 as a quantitative criterion, greatly reducing the error of classification by human judgement. Sdr is defined as follows [40]:

$$Sdr = \frac{1}{A} \left[\iint_A \left(\sqrt{1 + \left(\frac{\partial z(x,y)}{\partial x} \right)^2 + \left(\frac{\partial z(x,y)}{\partial y} \right)^2} - 1 \right) dx dy \right], \quad (1)$$

where A is the area of the target region and $|Z_{(x,y)}|$ is the absolute value of the difference between the height of the mean plane and the height of the convex portion or the depth of the concave portion. The internal macro-defects and porosity were analyzed using X-ray computed tomography (CT), and the absolute density was measured using Archimedes' principle [41] as expressed in Equation (2):

$$\rho_{Ti-6Al-4V} = \frac{m_{Ti-6Al-4V} \bullet \rho_{water}}{m_{cTi-6Al-4V} - m_c}, \quad (2)$$

where $\rho_{water} = 0.9982$ g/cm³ is the density of the water at 20 °C and $m_{cTi-6Al-4V} = m_c + m_{Ti-6Al-4V}$, where $m_{Ti-6Al-4V}$ is the mass of the Ti-6Al-4V alloy in the air. Further, m_c is the sum of the masses of the container, water, and the submerged component supports. The relative density was calculated using the density of the rolled Ti-6Al-4V alloy (4.41 g/cm³), as calculated from the equation $\left(\frac{\rho_{Ti-6Al-4V}}{4.41} \right) \times 100\%$. Field-emission scanning electron microscopy (FE-SEM, JEOL JSM-IT800) with electron backscattered diffraction detector (EBSD, TSL TexSEM), and transmission electron microscopy (TEM, JEOL JEM-ARM200F) were used to characterize the microstructure. The EBSD data were analyzed using the OIM software (EDAX-TSL). SEM and X-ray CT were used to reveal the fracture-type. Tensile samples were selected from the middle part of the cube and tested at room temperature at a strain rate of 0.001 s⁻¹, using an Instron tensile machine.

2.4. Numerical simulations

CFD is a computational approach for solving the equations of thermo-fluid dynamics, involving the mass (3), momentum (4) and energy (5) conservation equations [42]:

$$\nabla \bullet \vec{v} = 0 \quad (3)$$

$$\frac{\partial \vec{v}}{\partial t} + (\vec{v} \bullet \nabla) \vec{v} = -\frac{1}{\rho} \nabla \vec{P} + \mu \nabla^2 \vec{v} + \vec{g} [1 - \alpha(T - T_m)] \quad (4)$$

$$\frac{\partial h}{\partial t} + (\vec{v} \bullet \nabla) h = \frac{1}{\rho} (\nabla \bullet k \nabla T) \quad (5)$$

Here, \vec{v} , \vec{P} and \vec{g} are the velocity vector, pressure and gravity vector, respectively. μ , α , ρ , h and k are the viscosity, thermal expansion coefficient, density, specific enthalpy and thermal conductivity, respectively. On this basis, a commercial computational CFD software, Flow 3D®, is used for 3D modelling of AM processes assisted by multi-scale correlated multi-physics field coupled numerical simulations. For the

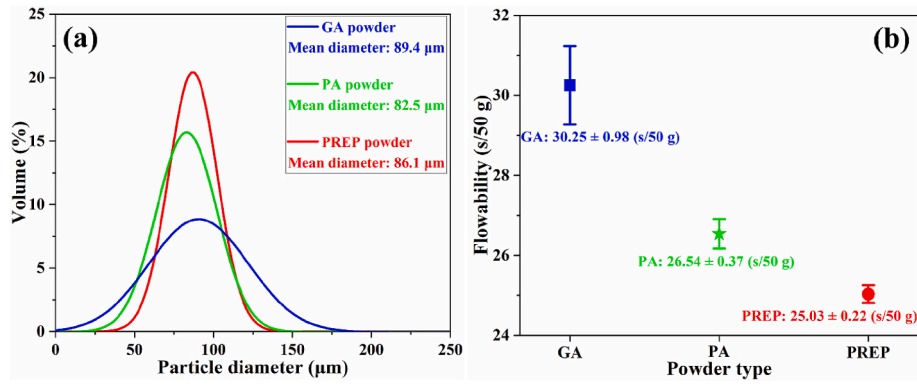


Fig. 2. (a) Particle size distribution (PSDs) and (b) flowability of GA, PA, and PREP Ti-6Al-4V alloy powders.

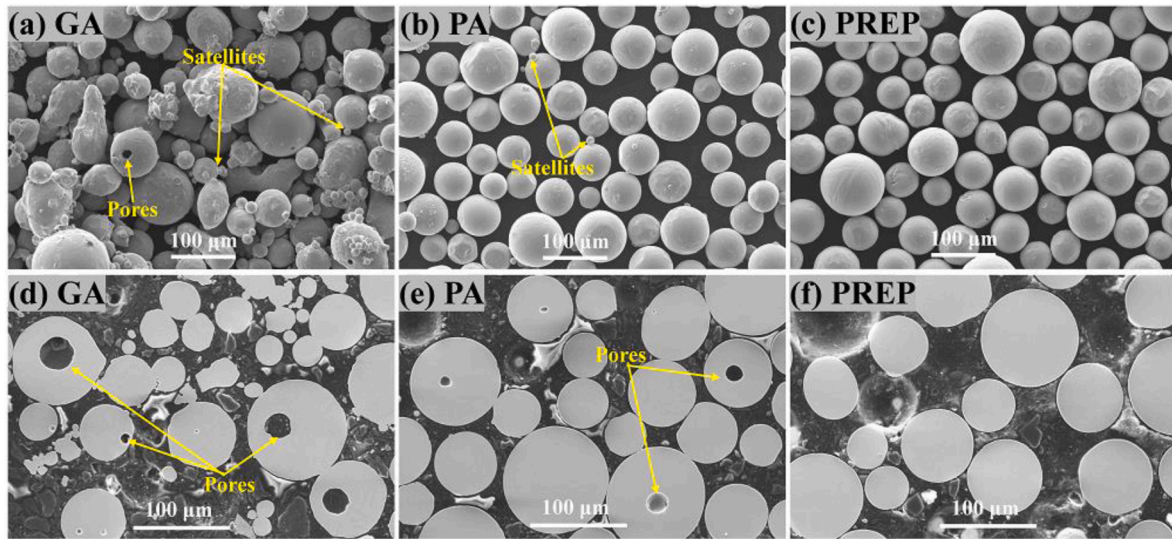


Fig. 3. SEM images of the surface morphology of Ti-6Al-4V alloy powders fabricated using (a) GA, (b) PA, and (c) PREP. SEM images of the cross-section of Ti-6Al-4V alloy powders fabricated by (d) GA, (e) PA, and (f) PREP.

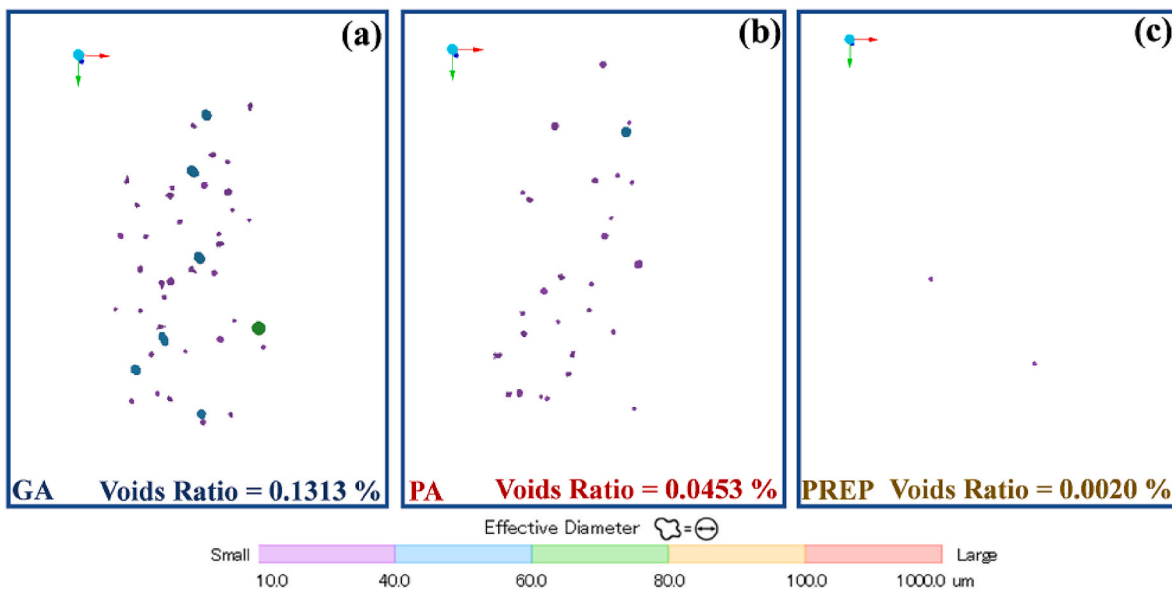


Fig. 4. X-ray CT measurements of (a) GA, (b) PA and (c) PREP powders of Ti-6Al-4V alloy. Internal voids are colored differently depending on their size.

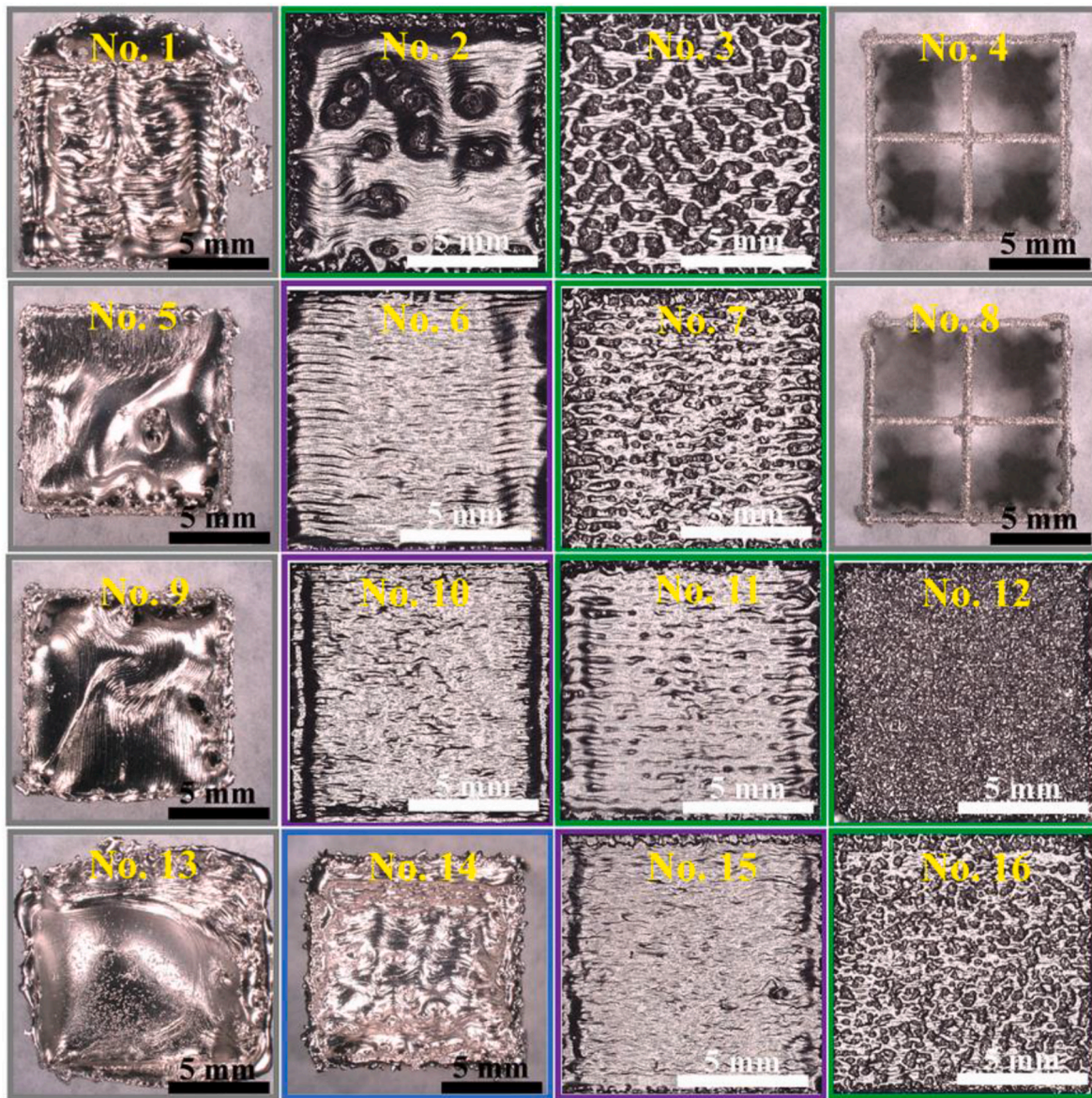


Fig. 5. Surface morphology of Ti-6Al-4V alloys with different printing parameters.

PBF-EB process, the heat source must be described as the energy input by the electron beam, which has an approximate Gaussian distribution as follows [43]:

$$q(r) = \frac{2\eta Q}{\pi r_0^2} \exp\left(-\frac{2r^2}{r_0^2}\right) \quad (6)$$

Here, r_0 and r are effective beam radius and actual spot radius, respectively. Q is beam power. η is energy efficiency at which the energy density decays to $1/e^2$ of the beam spot center. In order to accurately describe the temperature variations and melt pool state of the PBF-EB process, the physical model is tailored to the specific alloy and printing conditions and incorporates the influences of capillary force, Marangoni force, and vapor recoil pressure into the simulation. Based on the thermal characteristics of the Ti-6Al-4V alloy, the specific conditions used in the simulations are shown in Table 2, and these characteristics are taken from the software database and some literatures [44,45]. More details on the physical properties and parameters of the model can be found in the literature [43,45].

2.5. Machine learning models

Support vector machine (SVM) techniques was used to construct processing maps to predict the internal macro-defects. It is a common method for dealing with binary classification problems. The SVM method has the following advantages: it can solve high-dimensional problems, i.e. large feature spaces; it solves machine learning problems with small samples; it is able to handle the interaction of non-linear features; there is no local minimal value problem; it has a relatively strong generalization ability, etc. And more details on the SVM method are provided in the Supplementary Material section. The basic idea behind SVM is to separate the input vectors by mapping them to a high-dimensional feature space using kernel functions and constructing hyperplanes based on their classification labels [46,47]. The schematic model map is shown in Fig. 1(c). The input vectors are the PBF-EB printing parameters (beam current, scan speed, line offset, and focus offset), and the classification label is the surface quality (good or bad).

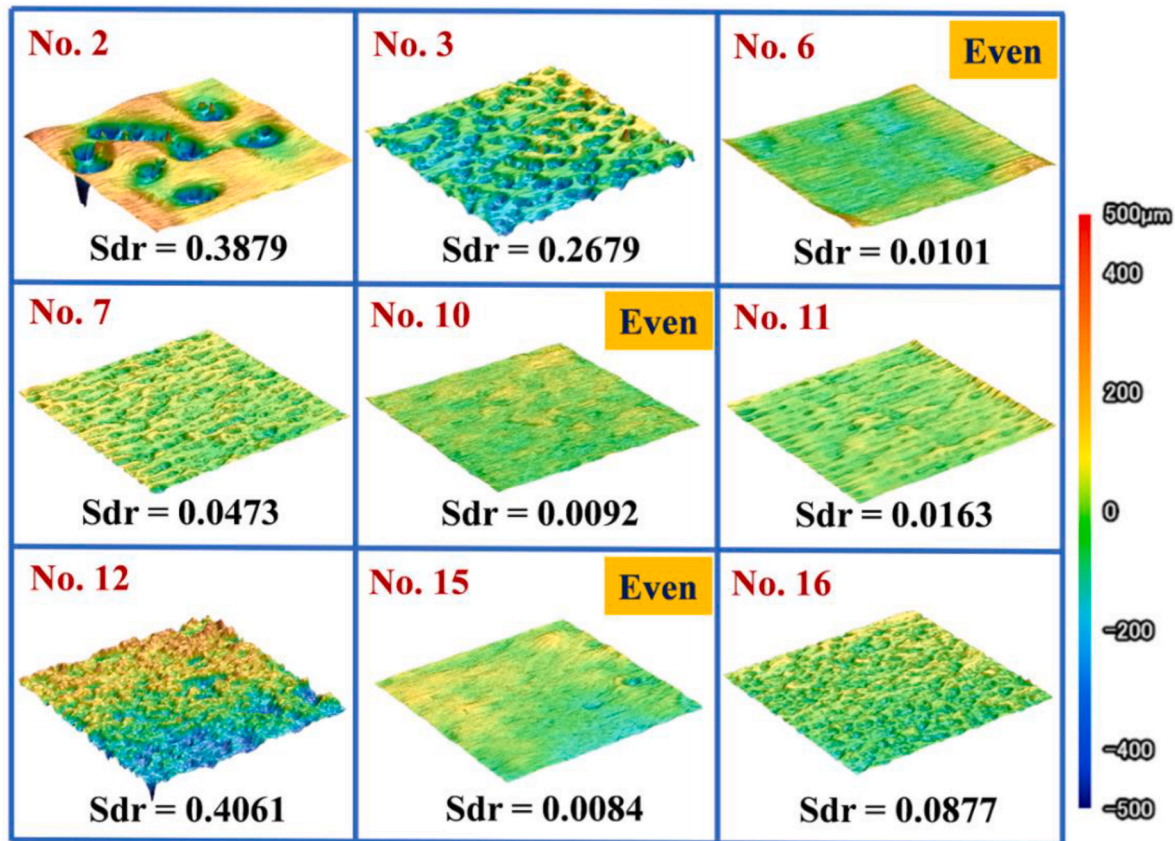


Fig. 6. Three-dimensional surface-topography images and surface roughness (Sdr) values with different printing parameters.

3. Results and discussion

3.1. Comparison of the characteristics of GA, PA, and PREP Ti-6Al-4V powders

The particle size distributions (PSDs) and flowability of the three types of Ti-6Al-4V alloy powders produced by GA, PA, and PREP are shown in Fig. 2. Although the average particle sizes are similar (89.4 μm for GA, 82.5 μm for PA, and 86.1 μm for PREP), the particle size range is different for the three types of powder (6.2–174.8 μm for GA, 27.3–139.2 μm for PA, and 39.4–133.9 μm for PREP). The flowability of the GA, PA, and PREP powders was 30.25 ± 0.98 , 26.54 ± 0.37 , and 25.03 ± 0.22 (s/50 g), respectively. The PREP powder exhibited the best flowability. These results indicate that a wider PSD provides less flowability, which may result in a low packing density of the powder bed. Fig. 3 shows the SEM micrographs of the surfaces and cross-sections of the three alloy powders. The GA powder exhibited poor sphericity, large amounts of satellite powder, and open pores (Fig. 3(a)). Solidified small powder particles collide with the unsolidified large particles under the impact of high-speed airflow and bond to their surface and co-solidify, leading to the formation of satellites [28]. Satellite powder affects powder flowability, which affects the formability of the powder bed. The PA powder has good sphericity; however, it contains a small amount of satellite powder (Fig. 3(b)), whereas the PREP powder has the best sphericity and contains no satellite powder (Fig. 3(c)). Cross-sectional images of the powders (Fig. 3(d–f)) revealed many pores in the GA powder, a few pores in the PA powder, and no pores in the PREP powder.

Fig. 4 shows the reconstructed X-ray CT images of the powders with pores labeled in different colors according to their sizes. The shape of the pores is spherical in all the powders, but the size of the pores is different for the three types of powders. The maximum diameter of the pores in the GA powders (Fig. 4(a)) reached 60–80 μm , and that in the PA

powders (Fig. 4(b)) reached 40–60 μm , whereas the maximum size of the pores in the PREP powders (Fig. 4(c)) did not exceed 40 μm , and was close to 10 μm . Porosity was also analyzed from the X-ray CT reconstructed data. It was found that the porosity of the GA, PA, and PREP Ti-6Al-4V powders was 0.1313%, 0.0453%, and 0.0020%, respectively. During the GA process, ultrasonic gas currents were applied to break up the continuous Ti-6Al-4V melt stream into spray droplets, and these gases entrapped inside the liquid droplets during solidification, leading to the formation of pores [28]. Similarly, in the PA process, Ti-6Al-4V wires were melted instantly by a plasma, and immediately broken into droplets by the ultrasonic gas stream from the nozzle [28]. In the PREP process, a rotating metal bar is melted by a plasma arc, and fine molten droplets are thrown out by high-speed centrifugal forces, which then solidify into powder particles, producing a spherical powder with a very low porosity [28]. Cunningham et al. showed that the gas pores trapped in the virgin powder would remain in the components constructed by PBF-EB [48]. One of the most important factors affecting the printability and part quality of Ti-6Al-4V alloys is the choice of the virgin powder. In this study, PREP powders with good flowability, high surface quality, and minimal porosity were used as the feedstock for the subsequent printing of Ti-6Al-4V parts without internal macro-defects.

3.2. Surface morphology and internal macro-defects in Ti-6Al-4V alloys

The PBF-EB process contains many process parameters. Inappropriate setting for either of them results in printed alloys with poor surface quality and internal macro-defects. Fig. 5 shows the optical images of the top surface of the 16 sets of Ti-6Al-4V alloys with different combinations of printing parameters (beam current, scan speed, line offset, and focus offset). It is possible to classify the surface quality of a sample as good or bad according to Fig. 5, with good surface quality being the presence of an even surface, and bad surface quality as being

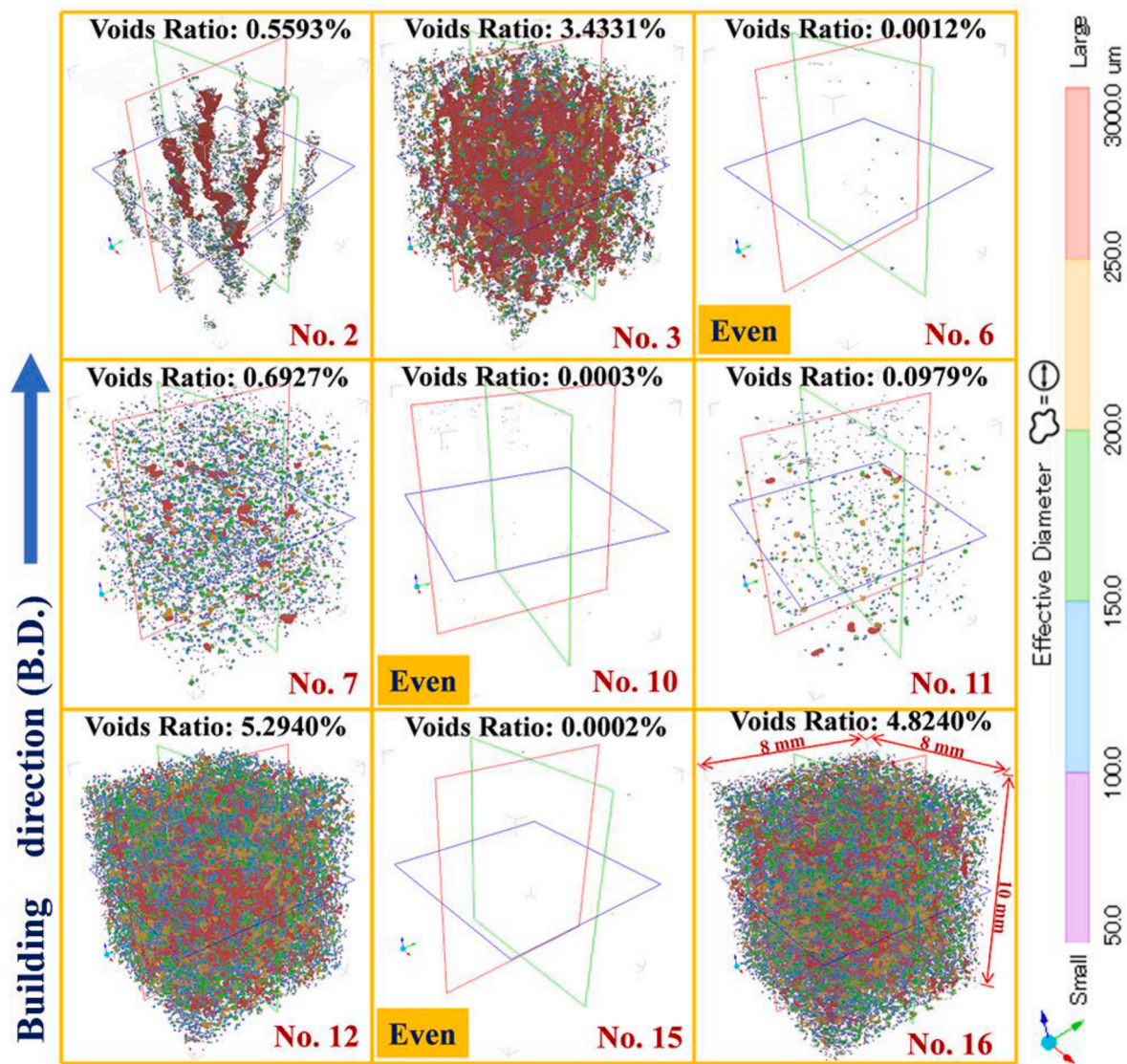


Fig. 7. Three-dimensional rendering of X-ray CT analysis, along with the void-ratio; internal voids are colored differently depending on their size.

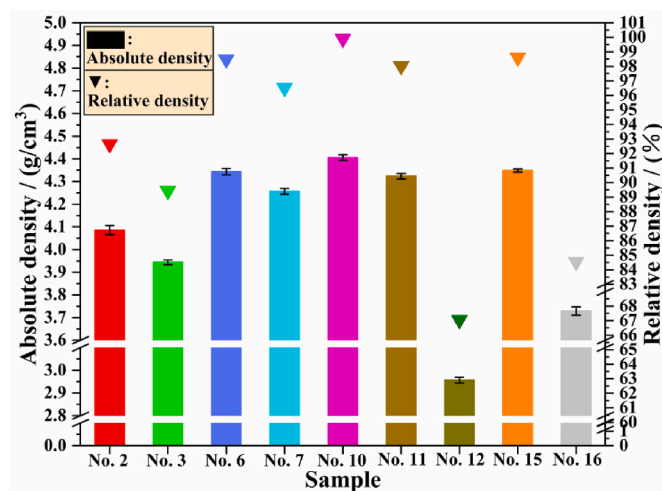
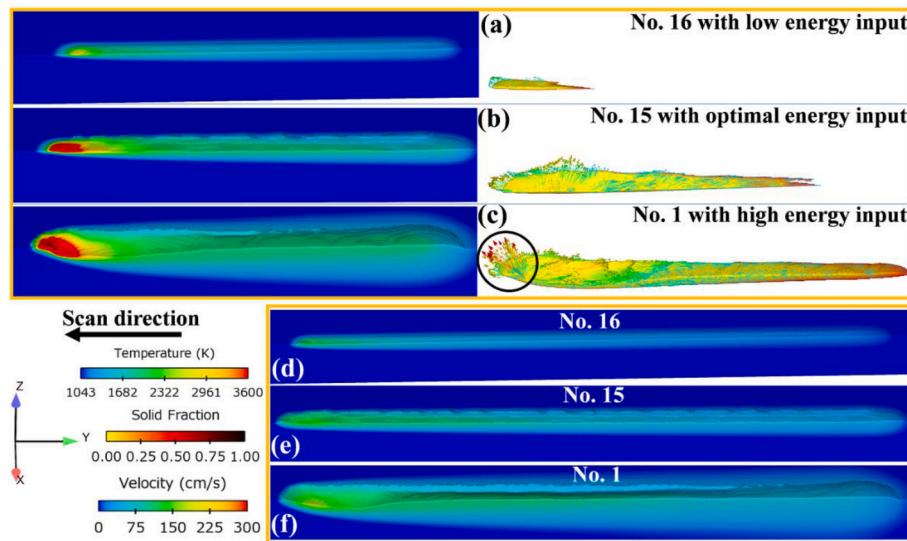


Fig. 8. Absolute and relative densities of Ti-6Al-4V alloys with different printing parameters.

subdivided into porous and uneven categories. Because of the low energy input in samples 4 and 8, the powder could not be melted and thus could not be printed successfully. Conversely, samples 1, 5, 9, 13, and 14 exhibited unstable melting due to excessive energy input, and their surfaces were uneven and therefore interrupted early. Among the remaining nine sets of samples printed to a height of 10 mm, samples 6, 10, and 15 showed an even surface; sample 2 showed an uneven surface; and samples 3, 7, 11, 12, and 16 showed porous surfaces. Fig. 6 shows the 3D surface topography and corresponding surface roughness (Sdr) values. Only the Sdr values for the central 10 × 10 mm² area of each sample were calculated to avoid disturbances from the edge contours. To evaluate the surface quality of the PBF-EB-processed Ti-6Al-4V alloy, Sdr was introduced as an indicator of surface roughness because it can be used to screen out the even surfaces [26]. The three samples with even surfaces (samples 6, 10, and 15) have low Sdr values (0.0101, 0.0092, and 0.0084, respectively), indicating that the criterion Sdr < 0.015 that has been used for the carbon steel [26] can also be used as a quantitative indicator to estimate the surface quality.

The X-ray CT results shown in Fig. 7 clearly indicate that the surface quality is related to internal macro-defects. Samples 6, 10, and 15, with good surface quality (even surface), contained no apparent internal macro-defects. In contrast, samples with poor surface quality (porous

**Table 3**

Sdr, surface morphology, class and label of different Ti-6Al-4V alloys. Each part was categorized into one of the two classes and labels according to the value of Sdr ('good' for Sdr < 0.015 and 'bad' otherwise). Ti-6Al-4V alloys with even surface are defined as 'good' and labeled as '1'. Ti-6Al-4V alloys with uneven and porous surfaces are defined as 'bad' and labeled as '0'.

Sample No.	Sdr	Surface Morphology	Class	Label
1	–	uneven	bad	0
2	0.3879	uneven	bad	0
3	0.2679	porous	bad	0
4	–	fail	bad	0
5	–	uneven	bad	0
6	0.0101	even	good	1
7	0.0473	porous	bad	0
8	–	fail	bad	0
9	–	uneven	bad	0
10	0.0092	even	good	1
11	0.0163	porous	bad	0
12	0.4061	porous	bad	0
13	–	uneven	bad	0
14	–	uneven	bad	0
15	0.0084	even	good	1
16	0.0877	porous	bad	0

and uneven surfaces) contained a high concentration of internal macro-defects, namely, irregularly shaped voids and spherical pores. A comparison of the overall 3D profile of the samples scanned by X-CT shows that samples with poor surface quality have internal macro-defects both throughout the sample and partially dispersed defects which can significantly compromise the mechanical properties of the sample. In Fig. 7, the internal macro-defects are marked with different colors according to their effective diameters. The effective diameter of the internal macro-defects in the samples with even surfaces was less than 100 μm , whereas that in the samples with poor surface quality reached 2500–3000 μm . In addition, the size of the defects was found to depend on their shape. Spherical defects were smaller than 200 μm , and some irregularly shaped defects had a size up to 3000 μm . Spherical defects are mainly caused by small amounts of porosity in the raw material powder. Irregularly shaped defects arise mainly from unsuitable printing parameters resulting in lack of fusion and unmelted powders, etc. These defects are also the main types of internal macro-defects focused on in this study. Fig. 7 reveals that the void-ratio in the even-surfaced samples (samples 6, 10, 15) ranged from 0.0002% to 0.0012%, whereas that in the bad surface-quality sample (sample 12) was the highest at 5.2940%. Moreover, the density of the printed parts (Fig. 8)

indicated that the samples with even surfaces (samples 6, 10, 15) showed a high relative density of ~99%, whereas the sample with bad surface quality (sample 12) had the lowest relative density of 67.04%. These results are in good agreement with the X-ray CT results (Fig. 7).

3.3. Linkage between printing parameters - energy input - surface quality - internal macro-defects in PBF-EB-processed Ti-6Al-4V alloys

3.3. Linkage between printing parameters - energy input - surface quality - internal macro-defects in PBF-EB-processed Ti-6Al-4V alloys

Revealing the relationship between printing parameters - energy input - surface quality - internal macro-defects will help to understand the process of PBF-EB and thus make it easier to control and predict PBF-EB-processed Ti-6Al-4V alloys without internal macro-defects. The line energies ($E_{line} = \frac{P}{v_{scan}}$) in Table 1 show that the printing parameters directly affect the levels of energy input, and that the differences in sample morphology for different printing parameters are essentially due to the differences in energy input. In order to simplify the model and focus on the effect of energy input on the melt pool behavior, CFD was used to simulate the dynamic behavior of a single-track melt pool with three levels of energy input, the results of which are shown in Fig. 9. The print parameters of samples Nos. 16, 15 and 1 were chosen as input parameters for the simulation and their line energies were: 0.07 J mm⁻¹, 0.18 J mm⁻¹ and 1.17 J mm⁻¹, representing three levels of low, medium and high energy input, respectively. Fig. 9a and b simulate temperature distribution and solid fraction with fluid flow velocity of melt pool at one moment in the printing process. When energy input is too low (Fig. 9 (a)), the melt pool is smaller and the temperature is lower compared to a suitable energy input (Fig. 9(b)), while with an excessively high energy input (Fig. 9(c)), the melt pool becomes very large and the temperature is higher. The strong dynamic flow caused by the high thermal gradient due to the high energy input creates a driving force on the melt oblique above direction (as shown by the black elliptical box in Fig. 9(c)), resulting in an uneven surface. The shape of the melt pool at the end of printing in Fig. 9d-f shows a stable melt pool with an even surface for the sample No. 15 with the suitable energy input. Fig. 9(d) shows that the surface of sample No. 16 is only slightly molten. For the PBF-EB process, the energy input is too low to allow the depth of the melt pool to penetrate the thickness of the powder layer, resulting in insufficient melting of the Ti-6Al-4V alloy powder in the bottom part of the layer. By accumulating layer by layer, this leads to the appearance of porous surfaces and internal macro-defects of unmelted powder and insufficient interlayer connections. Fig. 9(f) shows the overheating and instability of the melt pool due to excessively high energy, resulting in a wavy surface of the sample No. 1 with a concave melt pool at the

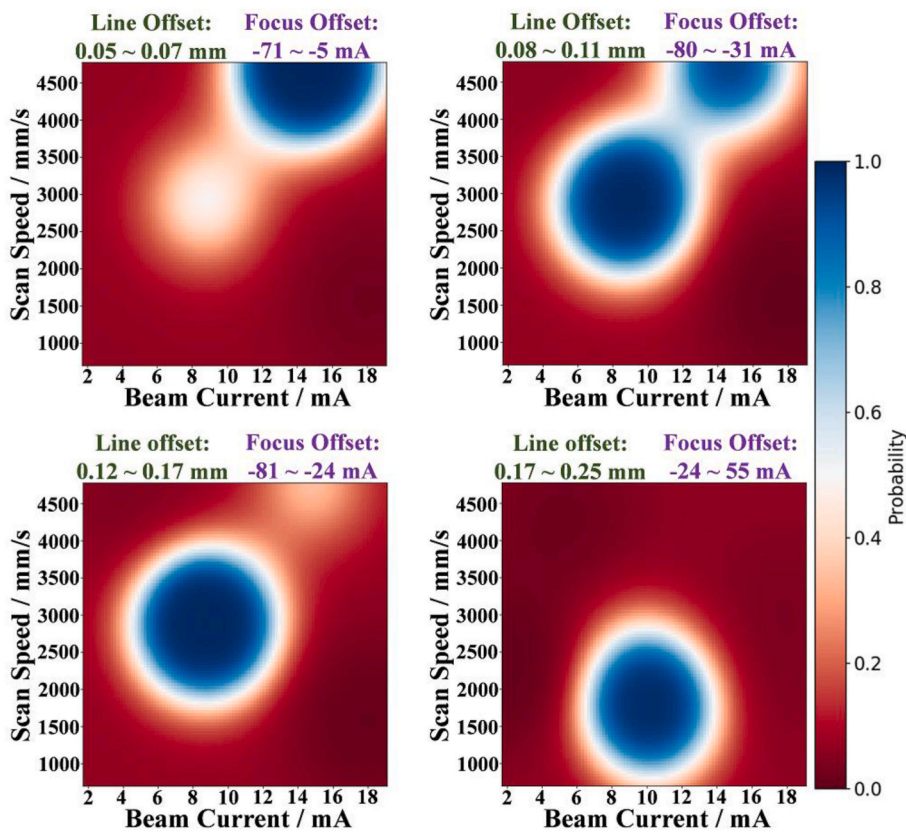


Fig. 10. Processing maps constructed using SVM as functions of four-dimensional printing parameters (i. e., beam current, scan speed, line offset, and focus offset). Blue areas indicate that the predicted surface morphology of the part printed using the corresponding process parameters is good (even) without internal macro-defects, whereas the red areas indicate a bad (uneven or porous) surface with internal macro-defects. (For interpretation of the references to color in this figure legend, the reader is referred to the Web version of this article.)

forward and a convex at the backside. During the spreading powder of PBF-EB layer by layer, concave or convex parts of the surface accumulate, eventually forming an uneven surface, while the uneven surface causes the thickness of the powder layers to vary, leading to insufficient interlayer connections and thus internal macro-defects.

3.4. Ti-6Al-4V alloys without internal macro-defects predicted by SVM

This section presents the idea of using SVM to determine the process window for providing defect-free Ti-6Al-4V alloys. The use of SVM converts the PBF-EB process problem to a binary classification problem with label values '1' and '0' that are used to represent two categories of the part quality, namely, 'good' (even defect-free surface) and 'bad' (uneven or porous surface with internal macro-defects), respectively. Table 3 shows the 16 sets of Ti-6Al-4V alloys after labelling the surface quality according to the Sdr criterion, where the labels with individual printing parameters (beam current, scan speed, line offset, and focus offset) were used as input datasets for the SVM model to create processing maps. The optimized cost parameter ($C = 0.7$) and hyperparameter ($\gamma = 1.5$) obtained by the grid-search method, and K -folder cross-validation optimizations were used as modelling parameters for the SVM processing map. Where the optimized cost parameter (C) indicates the importance given to a small number of outlier samples in the optimization problem. When C tends to infinity, the problem is also one where no samples with classification errors are allowed to exist, then it is an overfitting problem. When C tends to zero, we are no longer concerned with correct classification, but simply require the interval to be as large as possible, then we will not get a meaningful solution and the algorithm will not converge, it is an underfitting problem. The hyperparameter (γ) is used to determine some of the parameters of the model, while the tuning of the model actually refers to adjusting the (γ), and the (γ varies from one type of model to another. K -folder cross-validation means that the samples are divided into K subsets and one subset at a time is selected as the test set and the rest as the training set. These

parameters have no physical meaning and are used to tune the machine learning model. A classification boundary was drawn in four-dimensional space, with axes as the printing parameters of the PBF-EB process (Fig. 10). The red areas represent the printing parameters yielding poor surface-quality samples (uneven or porous surfaces) with internal macro-defects, and the blue areas represent the printing parameters for good surface-quality samples (even surface) without internal macro-defects.

3.5. Microstructures, mechanical properties, and fracture mechanisms of Ti-6Al-4V alloys

The microstructures of were systematically investigated. The EBSD and TEM results for sample 6, which was fabricated under the conditions represented by the blue area in Fig. 10, are shown in Figs. 11 and 12, respectively. The typical microstructure can be observed in the IPF map (Fig. 11 (a)), as a columnar primary β -grain pattern along the building direction. In the PBF-EB process, except immediately above the baseplate, the Ti-6Al-4V alloy was deposited on the same material in a layer-by-layer manner. In general, the heat conduction direction is almost parallel to the building direction, and the thermal gradient at the solidification front is large [49]. Therefore, columnar grains can often grow in the direction of heat conduction, resulting in columnar β grains growing along the building direction. The IPF and phase maps in Fig. 11 (b-d) reveal that the main phases within the columnar grains of the PBF-EB-processed Ti-6Al-4V alloy were the lamellar α phase and the fine β phase interspersed between the α lamellae. In sample 6, from the top toward the bottom positions (Fig. 11(b-d)), both the lamellar α and β phases become thicker as the distance from the baseplate decreases. The KAM diagram in Fig. 11(b-d) shows that the dislocation density gradually decreases from the top toward the bottom because the dislocation is mainly distributed at the phase boundaries of the α phase. The main reason for the difference in microstructure between the top, middle, and bottom parts of the sample is the in-situ heat treatment effect during the

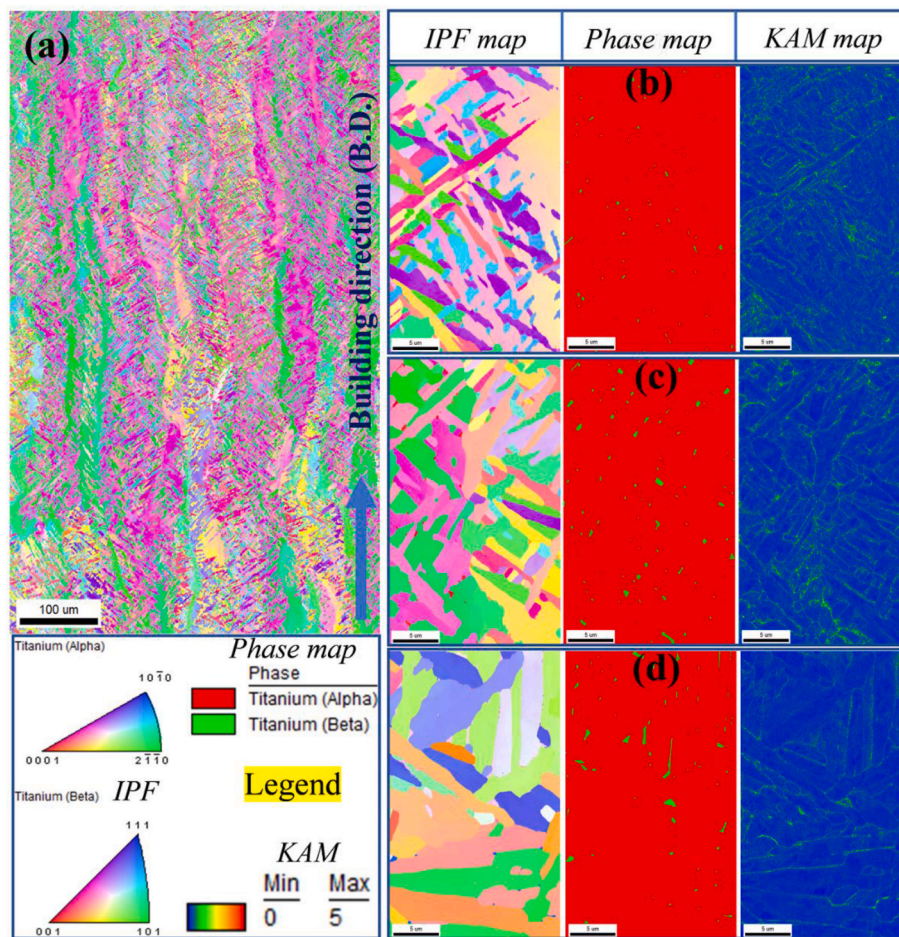


Fig. 11. EBSD maps of sample 6 fabricated under the processing conditions represented by the blue area in Fig. 11. (a) IPF map along the building direction. IPF, phase, and KAM maps obtained from EBSD at three different positions: (b) top, (c) middle, and (d) bottom. (For interpretation of the references to color in this figure legend, the reader is referred to the Web version of this article.)

PBF-EB process.

Fig. 12(a–c) show the TEM bright field (BF) and dark field (DF) images, along with the selected area electron diffraction (SAED) pattern. The images were obtained from the middle portion of sample 6. These TEM images show both the α and β phases, with lamellar α phases in the bright areas of the dark-field images. Fig. 12(d) shows the BF-STEM image and the corresponding EDS elemental maps of Ti, Al, V, and Fe, for the elliptical portion outlined in Fig. 12(a). The bright yellow and bright red areas in the V and Fe elemental maps correspond to the β phase. The microstructure in this study can evolve as follows: at the beginning of the solidification, the liquid phase transforms into the β phase; during rapid solidification, the β phase transforms into the martensitic α' phase. During the building process, the solidified part is subjected to in-situ heat treatment at a building temperature of ~ 1043 K, and the martensitic α' phase transforms into $\alpha + \beta$ phases. This microstructural evolution can be summarized as $L \rightarrow \beta \rightarrow \alpha' \rightarrow \alpha + \beta$, which is similar to the previously reported microstructural evolution of the Ti–6Al–4V alloy prepared via PBF-EB technology [12,50–52].

Fig. 13(a) shows the engineering stress–strain curves for the samples 6, 10, and 15, the samples without internal macro-defects, fabricated under the processing conditions represented by the blue area in Fig. 10, and also for the representative samples 3 and 11 with different types of internal macro-defects, fabricated using the processing conditions represented by the red area in Fig. 10. Defect-free samples (6, 10, and 15) shown in Fig. 13(a) show excellent elongation. Among them, sample 6 exhibited the best mechanical properties, with an ultimate tensile strength (UTS) of 934.7 MPa and elongation-to-failure (EL) of 24.3%.

The elongation of the three defect-free samples is much higher than that of the previously reported samples fabricated by PBF-EB, PBF-LB, and DED-LB [12,53–65] as shown in Fig. 13(b). Because the microstructures in Figs. 11 and 12 are not significantly different from those of the previously reported Ti–6Al–4V alloy prepared by PBF-EB, the high elongation in this study is mainly attributable to the elimination of internal macro-defects. Sample 3 fractured before the applied stress reached the yield strength, and sample 11 reached the yield strength but failed prematurely in the plastic stage. Fig. 14(a–c) show the results of the X-CT analysis for the representative samples 3, 11, and 6 before and after the tensile test. Fig. 14(d–f) show the corresponding fracture surface morphologies of the three samples after the tensile test. Samples 3 and 11 in Fig. 14 (a) and 14 (b) contained many irregular-shaped defects due to the lack of fusion, which caused premature fracture. In contrast, sample 6 in Fig. 14 (c) contained no defects, and a clear dimple pattern could be observed on the fractured surface. During the deformation process, the lack-of-fusion-type defects (Fig. 14 (d) and 14 (f)) could easily initiate multiple cracks, leading to premature fracture of the sample. Voids resulting from the lack-of-fusion tend to be larger and show an irregular shape (Fig. 14 (b) and 14 (e)), and these voids are generally distributed in the boundary zone of two adjacent layers or are perpendicular to the building direction. When subjected to uniaxial tensile loads parallel to the building direction, the sharp corners of the edges of these voids typically generated concentrated local stresses, leading to premature failure. The lack-of-fusion-type defects are fatal to the performance of AM products. These arise mainly as a result of deviations from the optimal processing conditions, leading to inadequate

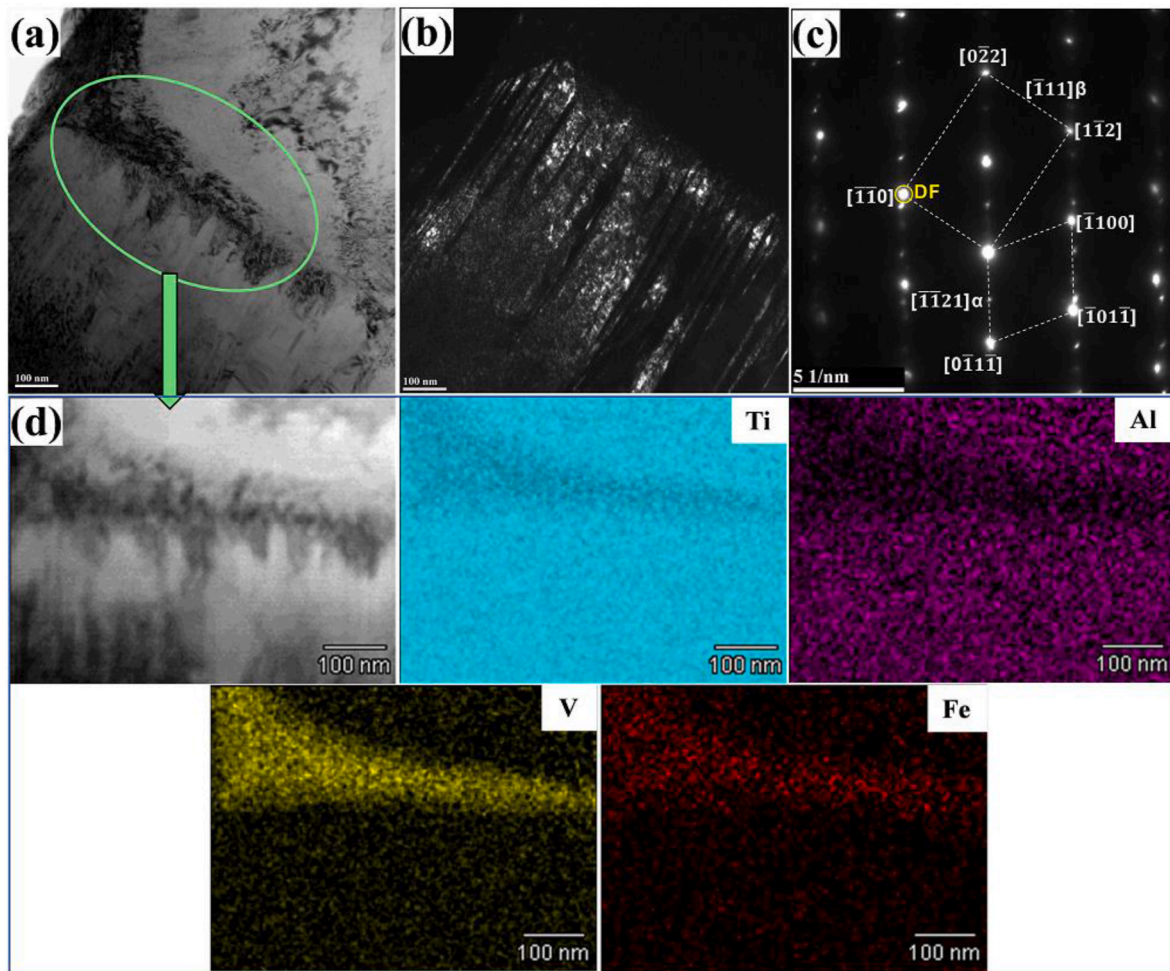


Fig. 12. (a) TEM bright field image, (b) corresponding dark field image, and (c) SAED pattern of sample 6 taken from the middle portion. (d) BF-STEM image and the corresponding EDS maps of Ti, Al, V and Fe for the green elliptical portion in (a). (For interpretation of the references to color in this figure legend, the reader is referred to the Web version of this article.)

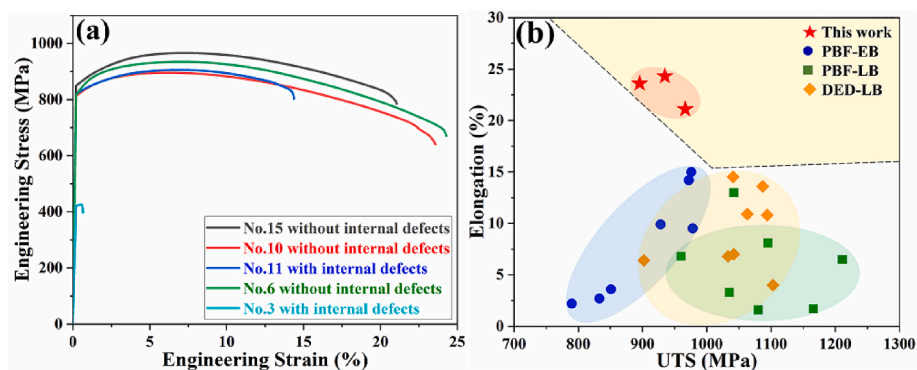


Fig. 13. Mechanical properties of the present Ti-6Al-4V alloys. (a) Engineering stress-strain tensile curves of Ti-6Al-4V alloys with different printing parameters at room temperatures. (b) Comparison of UTS and elongation with PBF-EB, PBF-LB, and DED-LB-fabricated Ti-6Al-4V alloys in literature [12,53–65].

melting and weak interlayer bonding. Therefore, the processing maps predicted by machine learning in this study can be used to efficiently obtain the process parameters for defect-free Ti-6Al-4V alloys with excellent elongation.

To clearly reveal the deformation mechanism of the PBF-EB-Ti6Al4V alloy, we investigated the microstructure of sample 6 after fracture, as shown in Fig. 15. It can be found from Fig. 15 (a) that the cracks mainly occur at the junction of the fine lamellar α phases. The KAM diagram in

Fig. 15 (b) clearly shows the low dislocation density in the α massive phase, with high dislocation density zones and cracks concentrated at the junctions of the lamellar α phases. As the degree of deformation increases, a large number of dislocations accumulate at the junction of the lamellar α -phase, and cracking occurs when the dislocations accumulate to a certain extent during further deformation, which has the effect of dislocation strengthening but reduces plasticity. While the α massive phase can effectively release stress through slip deformation,

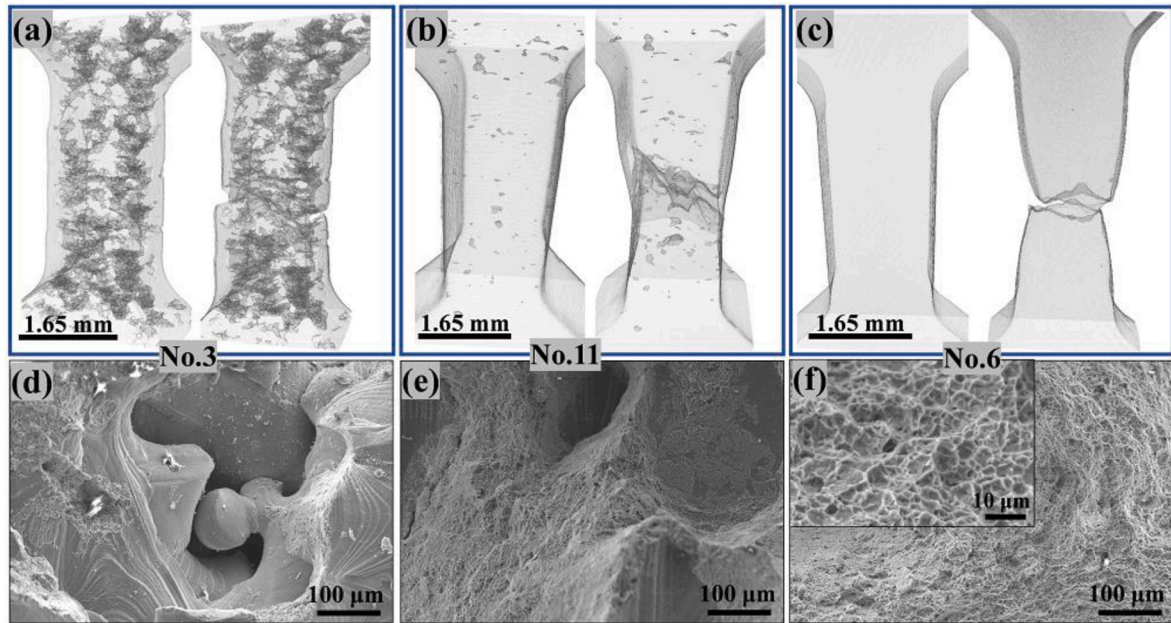


Fig. 14. X-ray CT measurements before and after the tensile test: (a) sample 3 with internal macro-defects, (b) sample 11 with internal macro-defects, and (c) sample 6 without internal macro-defects. (d), (e), (f) show the SEM morphology of fractured surfaces corresponding to (a), (b), and (c), respectively.

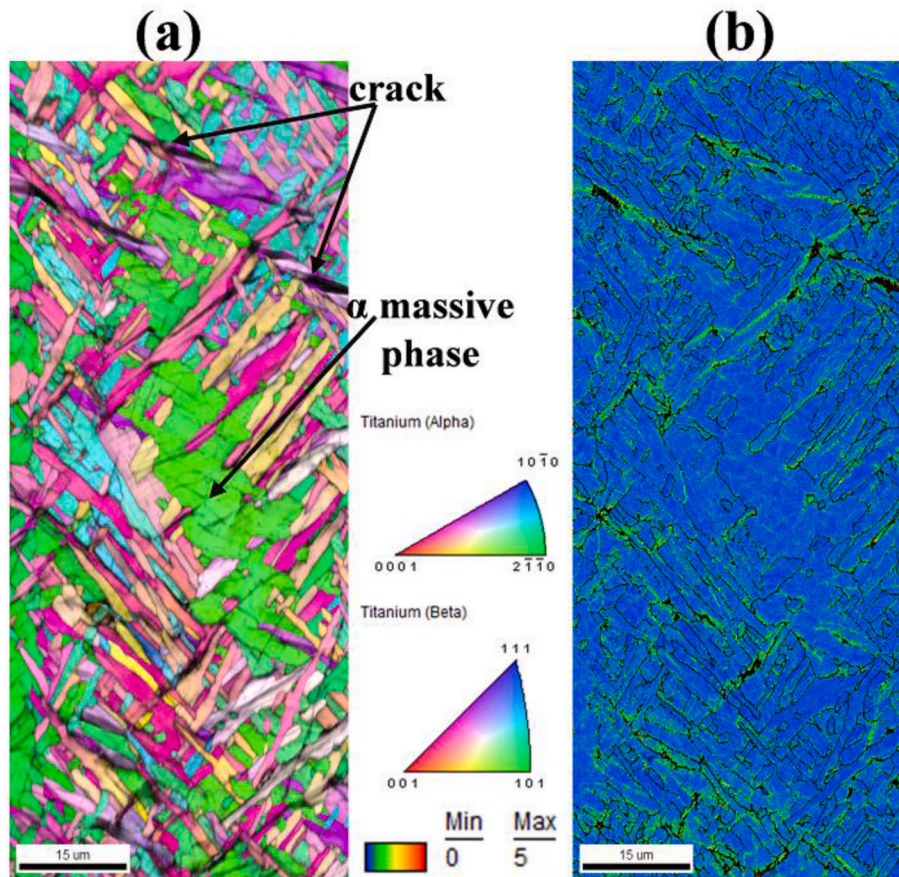


Fig. 15. EBSD maps of sample 6 along the building and tensile direction after fracture. (a) IPF + IQ map, and (b) KAM map.

reduce dislocation plugging and increase plasticity. In future research, strength and plasticity can be regulated by modulating the proportion of lamellar α phase and α massive phase.

4. Conclusions

The characteristics of the three types of Ti-6Al-4V alloy powders produced via GA, PA, and PREP were compared. The PREP powder with

the best sphericity, flowability, and low porosity was found to be the most favorable powder for subsequent printing of Ti-6Al-4V alloys without internal macro-defects. The quantitative criterion of Sdr <0.015 for even surfaces was also found to be applicable to Ti-6Al-4V alloys. The process maps of Ti-6Al-4V alloys include two regions, high beam current/scan speed and low beam current/scan speed, both of which have similar energy inputs because the building quality of the sample is primarily related to the energy input. The defect-free sample exhibited good elongation (24.3%), which was much higher than that previously reported for the additively manufactured Ti-6Al-4V alloy. The high elongation is mainly attributed to the elimination of internal macro-defects. This processing map predicts a processing window with a wide range of four-dimensional printing parameters, which also offers the possibility of subsequent development of higher-performance Ti-6Al-4V alloys without internal macro-defects.

CRedit authorship contribution statement

Yunwei Gui: Writing – original draft, Visualization, Validation, Investigation. **Kenta Aoyagi:** Writing – review & editing, Supervision, Resources, Methodology, Funding acquisition, Conceptualization. **Aki-hiko Chiba:** Supervision, Funding acquisition.

Declaration of competing interest

The authors declare that they have no known competing financial interests or personal relationships that could have appeared to influence the work reported in this paper.

Data availability

The authors are unable or have chosen not to specify which data has been used.

Acknowledgments

This study was based on the results obtained from project JPNP19007, commissioned by the New Energy and Industrial Technology Development Organization (NEDO). This work was also supported by JSPS KAKENHI (Proposal No. 21K03801) and the Inter-University Cooperative Research Program (Proposal nos. 18G0418, 19G0411, and 20G0418) of the Cooperative Research and Development Center for Advanced Materials, Institute for Materials Research, Tohoku University. It was also supported by the Council for Science, Technology, and Innovation (CSTI), Cross-ministerial Strategic Innovation Promotion Program (SIP), “Materials Integration” for the Revolutionary Design System of Structural Materials (Funding Agency: JST). Yunwei Gui acknowledges financial support from the China Scholarship Council (Grant No. 201908410208).

Appendix A. Supplementary data

Supplementary data to this article can be found online at <https://doi.org/10.1016/j.msea.2023.144595>.

References

- [1] S. Shao, M.M. Khonsari, S. Guo, W.J. Meng, N. Li, Overview: additive manufacturing enabled accelerated design of Ni-based alloys for improved fatigue life, *Addit. Manuf.* 29 (2019), <https://doi.org/10.1016/j.addma.2019.100779>.
- [2] M. Galati, L. Iuliano, A literature review of powder-based electron beam melting focusing on numerical simulations, *Addit. Manuf.* 19 (2018) 1–20, <https://doi.org/10.1016/j.addma.2017.11.001>.
- [3] C. Körner, Additive manufacturing of metallic components by selective electron beam melting - a review, *Int. Mater. Rev.* 61 (2016) 361–377, <https://doi.org/10.1080/09506608.2016.1176289>.
- [4] T. DeRoy, H.L. Wei, J.S. Zuback, T. Mukherjee, J.W. Elmer, J.O. Milewski, A. M. Beese, A. Wilson-Heid, A. De, W. Zhang, Additive manufacturing of metallic

- components – process, structure and properties, *Prog. Mater. Sci.* 92 (2018) 112–224, <https://doi.org/10.1016/j.pmatsci.2017.10.001>.
- [5] T.A. Rodrigues, J.D. Escobar, J. Shen, V.R. Duarte, G.G. Ribamar, J.A. Avila, E. Maawad, N. Schell, T.G. Santos, J.P. Oliveira, Effect of heat treatments on 316 stainless steel parts fabricated by wire and arc additive manufacturing: microstructure and synchrotron X-ray diffraction analysis, *Addit. Manuf.* 48 (2021), 102428, <https://doi.org/10.1016/j.addma.2021.102428>.
- [6] X. Zuo, W. Zhang, Y. Chen, J. Oliveira, Z. Zeng, Y. Li, Z. Luo, S. Ao, Wire-based Directed Energy Deposition of NiTiTa shape memory alloys: microstructure, phase transformation, electrochemistry, X-ray visibility and mechanical properties, *Addit. Manuf.* 59 (2022), 103115, <https://doi.org/10.1016/j.addma.2022.103115>.
- [7] H.L. Wei, T. Mukherjee, W. Zhang, J.S. Zuback, G.L. Knapp, A. De, T. DeRoy, Mechanistic models for additive manufacturing of metallic components, *Prog. Mater. Sci.* 116 (2021), <https://doi.org/10.1016/j.pmatsci.2020.100703>.
- [8] Y. Gui, H. Bian, K. Aoyagi, A. Chiba, Microstructure evolution and hardness of S30C carbon steel produced by powder bed fusion using an electron beam and subsequent heat treatments, *Mater. Lett.* 328 (2022), 133096, <https://doi.org/10.1016/j.matlet.2022.133096>.
- [9] C.A.F. Salvador, E.L. Maia, F.H. Costa, J.D. Escobar, J.P. Oliveira, A compilation of experimental data on the mechanical properties and microstructural features of Ti-alloys, *Sci. Data* 9 (2022), <https://doi.org/10.1038/s41597-022-01283-9>, 1–6.
- [10] B. Callegari, J.P. Oliveira, K. Aristizabal, R.S. Coelho, P.P. Brito, L. Wu, N. Schell, F. A. Soldara, F. Mücklich, H.C. Pinto, In-situ synchrotron radiation study of the aging response of Ti-6Al-4V alloy with different starting microstructures, *Mater. Char.* 165 (2020), <https://doi.org/10.1016/j.matchar.2020.110400>.
- [11] A. du Plessis, Effects of process parameters on porosity in laser powder bed fusion revealed by X-ray tomography, *Addit. Manuf.* 30 (2019), 100871, <https://doi.org/10.1016/j.addma.2019.100871>.
- [12] S. Liu, Y.C. Shin, Additive manufacturing of Ti6Al4V alloy: a review, *Mater. Des.* 164 (2019), 107552, <https://doi.org/10.1016/j.matdes.2018.107552>.
- [13] D. Ren, S. Li, H. Wang, W. Hou, Y. Hao, W. Jin, R. Yang, R.D.K. Misra, L.E. Murr, Fatigue behavior of Ti-6Al-4V cellular structures fabricated by additive manufacturing technique, *J. Mater. Sci. Technol.* 35 (2019) 285–294, <https://doi.org/10.1016/j.jmst.2018.09.066>.
- [14] X. Ding, Y. Koizumi, K. Aoyagi, T. Kii, N. Sasaki, Y. Hayasaka, K. Yamanaka, A. Chiba, Microstructural control of alloy 718 fabricated by electron beam melting with expanded processing window by adaptive offset method, *Mater. Sci. Eng.* 764 (2019), 138058, <https://doi.org/10.1016/j.msea.2019.138058>.
- [15] R. Snell, S. Tammam-Williams, L. Chechik, A. Lyle, E. Hernández-Nava, C. Boig, G. Panoutsos, I. Todd, Methods for rapid pore classification in metal additive manufacturing, *JOM (J. Occup. Med.)* 72 (2020) 101–109, <https://doi.org/10.1007/s11837-019-03761-9>.
- [16] C. Panwisawas, C.L. Qiu, Y. Sovani, J.W. Brooks, M.M. Attallah, H.C. Basoalto, On the role of thermal fluid dynamics into the evolution of porosity during selective laser melting, *Scripta Mater.* 105 (2015) 14–17, <https://doi.org/10.1016/J.SCRIPAMAT.2015.04.016>.
- [17] J. Cai, F. Li, T. Liu, B. Chen, M. He, Constitutive equations for elevated temperature flow stress of Ti-6Al-4V alloy considering the effect of strain, *Mater. Des.* 32 (2011) 1144–1151, <https://doi.org/10.1016/j.matdes.2010.11.004>.
- [18] M. Simonelli, Y.Y. Tse, C. Tuck, The formation of $\alpha + \beta$ microstructure in as-fabricated selective laser melting of Ti-6Al-4V, *J. Mater. Res.* 29 (2014) 2028–2035, <https://doi.org/10.1557/jmr.2014.166>.
- [19] A. Gupta, C.J. Bennett, W. Sun, The role of defects and characterisation of tensile behaviour of EBM Additive manufactured Ti-6Al-4V: an experimental study at elevated temperature, *Eng. Fail. Anal.* 120 (2021), 105115, <https://doi.org/10.1016/j.engfailanal.2020.105115>.
- [20] B. Shen, H. Li, S. Liu, J. Zou, S. Shen, Y. Wang, T. Zhang, D. Zhang, Y. Chen, H. Qi, Influence of laser post-processing on pore evolution of Ti-6Al-4V alloy by laser powder bed fusion, *J. Alloys Compd.* 818 (2020), 152845, <https://doi.org/10.1016/j.jallcom.2019.152845>.
- [21] J. Benzing, N. Hrabe, T. Quinn, R. White, R. Rentz, M. Ahlfors, Hot isostatic pressing (HIP) to achieve isotropic microstructure and retain as-built strength in an additive manufacturing titanium alloy (Ti-6Al-4V), *Mater. Lett.* 257 (2019), 126690, <https://doi.org/10.1016/j.matlet.2019.126690>.
- [22] H. Gong, K. Rafi, H. Gu, T. Starr, B. Stucker, Analysis of defect generation in Ti-6Al-4V parts made using powder bed fusion additive manufacturing processes, *Addit. Manuf.* 1–4 (2014) 87–98, <https://doi.org/10.1016/J.ADDMA.2014.08.002>.
- [23] N. Sanaei, A. Fatemi, Defects in additive manufactured metals and their effect on fatigue performance: a state-of-the-art review, *Prog. Mater. Sci.* 117 (2021), 100724, <https://doi.org/10.1016/j.pmatsci.2020.100724>.
- [24] J. Schwerdtfeger, R.F. Singer, C. Körner, In situ flaw detection by IR-imaging during electron beam melting, *Rapid Prototyp. J.* 18 (2012) 259–263, <https://doi.org/10.1108/13552541211231572>.
- [25] N. Boone, C. Zhu, C. Smith, I. Todd, J.R. Willmott, Thermal near infrared monitoring system for electron beam melting with emissivity tracking, *Addit. Manuf.* 22 (2018) 601–605, <https://doi.org/10.1016/J.ADDMA.2018.06.004>.
- [26] Y. Gui, K. Aoyagi, H. Bian, A. Chiba, Detection, classification and prediction of internal defects from surface morphology data of metal parts fabricated by powder bed fusion type additive manufacturing using an electron beam, *Addit. Manuf.* 54 (2022), 102736, <https://doi.org/10.1016/j.addma.2022.102736>.
- [27] E. Muzangaza, The Effects of Titanium Ti-6Al-4V Powders Manufactured Using Electron Beam Melting (EBM) - Additive Manufacturing on Metallurgical Evaluation, Ph.D. Univ. Birmingham., 2018.
- [28] G. Chen, S.Y. Zhao, P. Tan, J. Wang, C.S. Xiang, H.P. Tang, A comparative study of Ti-6Al-4V powders for additive manufacturing by gas atomization, plasma rotating

- electrode process and plasma atomization, *Powder Technol.* 333 (2018) 38–46, <https://doi.org/10.1016/j.powtec.2018.04.013>.
- [29] P. Wang, M.L. Sharon Nai, X. Tan, G. Vastola, S. Raghavan, W.J. Sin, S.B. Tor, Q. X. Pei, J. Wei, Recent progress of additive manufactured Ti-6Al-4V by electron beam melting, *Solid Free, Fabr. 2016 Proc. 27th Annu. Int. Solid Free. Fabr. Symp. - An Addit. Manuf. Conf. SFF 2016* (2016) 691–704.
- [30] J. Ran, F. Jiang, X. Sun, Z. Chen, C. Tian, H. Zhao, Microstructure and mechanical properties of ti-6al-4v fabricated by electron beam melting, *Crystals* 10 (2020) 1–18, <https://doi.org/10.3390/cryst10110972>.
- [31] C. Qiu, C. Panwisawas, M. Ward, H.C. Basoalto, J.W. Brooks, M.M. Attallah, On the role of melt flow into the surface structure and porosity development during selective laser melting, *Acta Mater.* 96 (2015) 72–79, <https://doi.org/10.1016/j.actamat.2015.06.004>.
- [32] S.M.J. Razavi, B. Van Hooreweder, F. Berto, Effect of build thickness and geometry on quasi-static and fatigue behavior of Ti-6Al-4V produced by Electron Beam Melting, *Addit. Manuf.* 36 (2020), 101426, <https://doi.org/10.1016/j.addma.2020.101426>.
- [33] M. Iebba, A. Astarita, D. Mistretta, I. Colonna, M. Liberini, F. Scherillo, C. Pirozzi, R. Borrelli, S. Franchitti, A. Squillace, Influence of powder characteristics on formation of porosity in additive manufacturing of Ti-6Al-4V components, *J. Mater. Eng. Perform.* 26 (2017) 4138–4147, <https://doi.org/10.1007/s11665-017-2796-2>.
- [34] S. Nasiri, M.R. Khosravani, Machine learning in predicting mechanical behavior of additively manufactured parts, *J. Mater. Res. Technol.* 14 (2021) 1137–1153, <https://doi.org/10.1016/j.jmrt.2021.07.004>.
- [36] N.S. Johnson, P.S. Vulimiri, A.C. To, X. Zhang, C.A. Brice, B.B. Kappes, A. P. Stebner, Invited review: machine learning for materials developments in metals additive manufacturing, *Addit. Manuf.* 36 (2020), <https://doi.org/10.1016/j.addma.2020.101641>.
- [37] C. Wang, X.P. Tan, S.B. Tor, C.S. Lim, Machine learning in additive manufacturing: state-of-the-art and perspectives, *Addit. Manuf.* 36 (2020), 101538, <https://doi.org/10.1016/j.addma.2020.101538>.
- [38] K. Aoyagi, H. Wang, H. Sudo, A. Chiba, Simple method to construct process maps for additive manufacturing using a support vector machine, *Addit. Manuf.* 27 (2019) 353–362, <https://doi.org/10.1016/j.addma.2019.03.013>.
- [39] K.T. Fang, D.K.J. Lin, Ch 4, Uniform experimental designs and their applications in industry, *Handb. Stat.* 22 (2003) 131–170, [https://doi.org/10.1016/S0169-7161\(03\)22006-X](https://doi.org/10.1016/S0169-7161(03)22006-X).
- [40] L. Pagani, A. Townsend, W. Zeng, S. Lou, L. Blunt, X.Q. Jiang, P.J. Scott, Towards a new definition of areal surface texture parameters on freeform surface: Re-entrant features and functional parameters, *Meas. J. Int. Meas. Confed.* 141 (2019) 442–459, <https://doi.org/10.1016/j.measurement.2019.04.027>.
- [41] A.S. For Testing M.C.B. on Metal Powders, M.P. Products, A.S. For Testing, M.S.B. 0. on Bearings, Standard Test Methods for Density of Compacted or Sintered Powder Metallurgy (PM) Products Using Archimedes' Principle, ASTM International, 2009. <https://books.google.co.jp/books?id=G3lyMwEACAAJ>.
- [42] Q. Chen, Y. Zhao, S. Strayer, Y. Zhao, K. Aoyagi, Y. Koizumi, A. Chiba, W. Xiong, A. C. To, Elucidating the effect of preheating temperature on melt pool morphology variation in Inconel 718 laser powder bed fusion via simulation and experiment, *Addit. Manuf.* 37 (2021), 101642, <https://doi.org/10.1016/j.addma.2020.101642>.
- [43] Y. Zhao, Y. Koizumi, K. Aoyagi, D. Wei, K. Yamanaka, A. Chiba, Melted pool behavior and effect of fluid flow on solidification conditions in selective electron beam melting (SEBM) of a biomedical Co-Cr-Mo alloy, *Addit. Manuf.* 26 (2019) 202–214, <https://doi.org/10.1016/j.addma.2018.12.002>.
- [44] B. W, G.P.M. Boivineau, C. Cagran, D. Doytier, V. Eyraud, M.-H. Nadal, Thermophysical properties of solid and liquid Ti-6Al-4V (TA6V) alloy, *Int J Thermophys.* 27 (2006) 507–529, <https://doi.org/10.1007/PL00021868>.
- [45] Y. Cui, Y. Zhao, H. Numata, H. Bian, K. Wako, K. Yamanaka, K. Aoyagi, C. Zhang, A. Chiba, Effects of plasma rotating electrode process parameters on the particle size distribution and microstructure of Ti-6Al-4 V alloy powder, *Powder Technol.* 376 (2020) 363–372, <https://doi.org/10.1016/j.powtec.2020.08.027>.
- [46] W.S. Noble, What is a support vector machine? *Nat. Biotechnol.* 24 (2006) 1565–1567, <https://doi.org/10.1038/nbt1206-1565>.
- [47] X. Huang, A. Maier, J. Hornegger, J.A.K. Suykens, Indefinite kernels in least squares support vector machines and principal component analysis, *Appl. Comput. Harmon. Anal.* 43 (2017) 162–172, <https://doi.org/10.1016/j.acha.2016.09.001>.
- [48] R. Cunningham, A. Nicolas, J. Madsen, E. Fodran, E. Anagnostou, M.D. Sangid, A. D. Rollett, Analyzing the effects of powder and post-processing on porosity and properties of electron beam melted Ti-6Al-4V, *Mater. Res. Lett.* 5 (2017) 516–525, <https://doi.org/10.1080/21663831.2017.1340911>.
- [49] Y. Zhao, Y. Koizumi, K. Aoyagi, K. Yamanaka, A. Chiba, Manipulating local heat accumulation towards controlled quality and microstructure of a Co-Cr-Mo alloy in powder bed fusion with electron beam, *Mater. Res. Lett.* 254 (2019) 269–272, <https://doi.org/10.1016/j.matlet.2019.07.078>.
- [50] M. Rashid, R.L. Narayan, D.L. Zhang, W.Z. Han, A comparative study of microstructures and mechanical behavior of laser metal deposited and electron beam melted Ti-6Al-4V, *J. Mater. Eng. Perform.* 31 (2022) 542–551, <https://doi.org/10.1007/s11665-021-06197-y>.
- [51] S.L. Lu, M. Qian, H.P. Tang, M. Yan, J. Wang, D.H. StJohn, Massive transformation in Ti-6Al-4V additively manufactured by selective electron beam melting, *Acta Mater.* 104 (2016) 303–311, <https://doi.org/10.1016/j.actamat.2015.11.011>.
- [52] X. Tan, Y. Kok, W.Q. Toh, Y.J. Tan, M. Descoins, D. Mangelinck, S.B. Tor, K. F. Leong, C.K. Chua, Revealing martensitic transformation and α/β interface evolution in electron beam melting three-dimensional-printed Ti-6Al-4V, *Sci. Rep.* 6 (2016) 1–10, <https://doi.org/10.1038/srep26039>.
- [53] Y. Zhai, H. Galarraga, D.A. Lados, Microstructure, static properties, and fatigue crack growth mechanisms in Ti-6Al-4V fabricated by additive manufacturing: LENS and EBM, *Eng. Fail. Anal.* 69 (2016) 3–14, <https://doi.org/10.1016/j.engfailanal.2016.05.036>.
- [54] M. Seifi, A. Salem, J. Beuth, O. Harrysson, J.J. Lewandowski, Overview of materials qualification needs for metal additive manufacturing, *JOM (J. Occup. Med.)* 68 (2016) 747–764, <https://doi.org/10.1007/s11837-015-1810-0>.
- [55] B.E. Carroll, T.A. Palmer, A.M. Beese, Anisotropic tensile behavior of Ti-6Al-4V components fabricated with directed energy deposition additive manufacturing, *Acta Mater.* 87 (2015) 309–320, <https://doi.org/10.1016/j.actamat.2014.12.054>.
- [56] P. Edwards, A. O'Conner, M. Ramulu, Electron beam additive manufacturing of titanium components: properties and performance, *J. Manuf. Sci. Eng. Trans. ASME.* 135 (2013) 1–7, <https://doi.org/10.1115/1.4025773>.
- [57] B. Wysocki, P. Maj, R. Sitek, J. Buhagiar, K.J. Kurzydowski, W. Świeszkowski, Laser and electron beam additive manufacturing methods of fabricating titanium bone implants, *Appl. Sci.* 7 (2017) 1–20, <https://doi.org/10.3390/app7070657>.
- [58] M. Koike, P. Greer, K. Owen, G. Lilly, L.E. Murr, S.M. Gaytan, E. Martinez, T. Okabe, Evaluation of titanium alloys fabricated using rapid prototyping technologies—electron beam melting and laser beam melting, *Materials* 4 (2011) 1776–1792, <https://doi.org/10.3390/ma4101776>.
- [59] L. Facchini, E. Magalini, P. Robotti, A. Molinari, S. Höges, K. Wissenbach, Ductility of a Ti-6Al-4V alloy produced by selective laser melting of prealloyed powders, *Rapid Prototyp. J.* 16 (2010) 450–459, <https://doi.org/10.1108/13552541011083371>.
- [60] H.K. Rafi, N.V. Karthik, H. Gong, T.L. Starr, B.E. Stucker, Microstructures and mechanical properties of Ti6Al4V parts fabricated by selective laser melting and electron beam melting, *J. Mater. Eng. Perform.* 22 (2013) 3872–3883, <https://doi.org/10.1007/s11665-013-0658-0>.
- [61] T. Vilaro, C. Colin, J.D. Bartout, As-fabricated and heat-treated microstructures of the Ti-6Al-4V alloy processed by selective laser melting, *Metall. Mater. Trans. A Phys. Metall. Mater. Sci.* 42 (2011) 3190–3199, <https://doi.org/10.1007/s11661-011-0731-y>.
- [62] J. Alcisto, A. Enriquez, H. Garcia, S. Hinkson, T. Steelman, E. Silverman, P. Valdivino, H. Gigerenzer, J. Foyos, J. Ogren, J. Dorey, K. Karg, T. McDonald, O. S. Es-Said, Tensile properties and microstructures of laser-formed Ti-6Al-4V, *J. Mater. Eng. Perform.* 20 (2011) 203–212, <https://doi.org/10.1007/s11665-010-9670-9>.
- [63] D.A. Hollander, M. Von Walter, T. Wirtz, R. Sellei, B. Schmidt-Rohlfing, O. Paar, H. J. Erli, Structural, mechanical and in vitro characterization of individually structured Ti-6Al-4V produced by direct laser forming, *Biomaterials* 27 (2006) 955–963, <https://doi.org/10.1016/j.biomaterials.2005.07.041>.
- [64] S. Leuders, M. Thöne, A. Riemer, T. Niendorf, T. Tröster, H.A. Richard, H.J. Maier, On the mechanical behaviour of titanium alloy TiAl6V4 manufactured by selective laser melting: fatigue resistance and crack growth performance, *Int. J. Fatig.* 48 (2013) 300–307, <https://doi.org/10.1016/j.ijfatigue.2012.11.011>.
- [65] P. Edwards, M. Ramulu, Fatigue performance evaluation of selective laser melted Ti-6Al-4V, *Mater. Sci. Eng.* 598 (2014) 327–337, <https://doi.org/10.1016/j.msea.2014.01.041>.